ADVANCED OPTICAL MATERIALS
www.advopticalmat.de

LIPSS for SERS: Metal Coated Direct Laser Written Periodic Nanostructures for Surface Enhanced Raman Spectroscopy

*Serena Nur Erkızan, Fırat İdikut, Özge Demirtaş, Arian Goodarzi, Ahmet Kemal Demir, Mona Borra, Ihor Pavlov, and Alpan Bek**

A novel method of fabricating large-area, low-cost surface-enhanced Raman spectroscopy (SERS) substrates is introduced which yields densely nanostructured surfaces utilizing laser-induced periodic surface structuring (LIPSS) of crystalline silicon (Si). Two different interaction regimes yield low spatial frequency (LSFL) and high spatial frequency (HSFL) LIPSS patterns. Nanostructuring of Si surface is followed by deposition of a thin noble metal layer to complete the fabrication procedure. A 50–70 nm thick Ag layer is shown to maximize the SERS performance. The SERS effect is attributed to the electromagnetic field enhancement originating from the nanoscale surface roughness of Si that can be controlled by LSFL and HSFL nature of the structure. The SERS substrates are found to be capable of detecting a Raman analyte down to 10^{-11} M. SERS performance of the Ag deposited substrates at 532, 660, and 785 nm excitation wavelengths is compared. Both LSFL and HSFL Si surfaces with 70 nm thick Ag are found to exhibit the strongest SERS under 660 nm excitation exhibiting Raman enhancement factors (EFs) as high as 10^9. The Raman EFs are calculated both by SERS spectra experimentally, and using finite-elements method simulation of the electric field enhancement where a good agreement is found.

1. Introduction

Surface-enhanced Raman spectroscopy (SERS) is a highly sensitive, nondestructive, label-free vibrational spectroscopic molecular identification technique that originates from the marriage of the high molecular specificity of Raman spectra and the ultra-high signal amplification property of plasmonic metal nanostructures.[1–8] SERS technique shows great promise in a wide variety of fields including biosensing, gas phase chemical detection, and single molecule detection.[9–15] Besides the high and spatially uniform enhancement factor (EF); chemical stability, reproducibility, precision, and fast fabrication in large areas with less debris are demanded for ideal SERS substrates.[16,17] Even though metallic nanoparticles exhibit high SERS EFs, they do not offer proper particle stability, and use in large areas.[18–20] Femtosecond laser-based techniques offer the fabrication of highly sensitive SERS substrates with low detection limits.[21–23] On the contrary to wet chemical synthesis procedures, uniformity, robustness, and reproducibility are provided by laser-assisted periodic nanostructures. Without any lithographic processes, the number of processes to fabricate highly sensitive SERS sensing devices is also reduced.[24–26]

Generation of laser-induced periodic surface structuring (LIPSS) by using the direct laser writing technique with ultrafast (femtosecond – fs) laser sources[27] is a fast and low-cost method compared to other well-established techniques such as laser interference lithography,[28] photolithography, electron beam lithography, and nanoimprint lithography.[29] Controlling the irradiation wavelength, the number of pulses on the spot, the polarization direction of the beam, repetition rate, the fluence of the ultrafast laser, and the scanning speed leads to the formation of the nano ripples on semiconductors and metals.[30–34] Nanoripples formed by an fs-laser can be classified into two, Low Spatial Frequency LIPSS (LSFL) and High Spatial Frequency LIPSS (HSFL).[35] Furthermore, both types of structures, formed on metal and semiconductor surfaces, have potential benefits as a SERS substrate as well.[36–41] LSFL structures exhibit periods close to irradiation wavelength, meanwhile; HSFL structures have periods smaller than half of the irradiation wavelength.[35,42–46] The formation mechanism of LSFL structures was first introduced by Sipe theory in 1982.[47] With the appropriate energy exposure and the high number of free carriers on the surface, the dielectric

S. N. Erkızan, F. İdikut, I. Pavlov, A. Bek
Physics Department
Middle East Technical University
Ankara 06800, Turkey
E-mail: bek@metu.edu.tr
Ö. Demirtaş, I. Pavlov, A. Bek
Micro and Nanotechnology Program
Middle East Technical University
Ankara 06800, Turkey
A. Goodarzi, M. Borra, I. Pavlov, A. Bek
ODTÜ-GÜNAM
The Center for Solar Energy Research and Applications
Ankara 06800, Turkey
A. K. Demir
Physics Department
Bilkent University
Ankara 06800, Turkey
The ORCID identification number(s) for the author(s) of this article can be found under https://doi.org/10.1002/adom.202200233.

DOI: 10.1002/adom.202200233

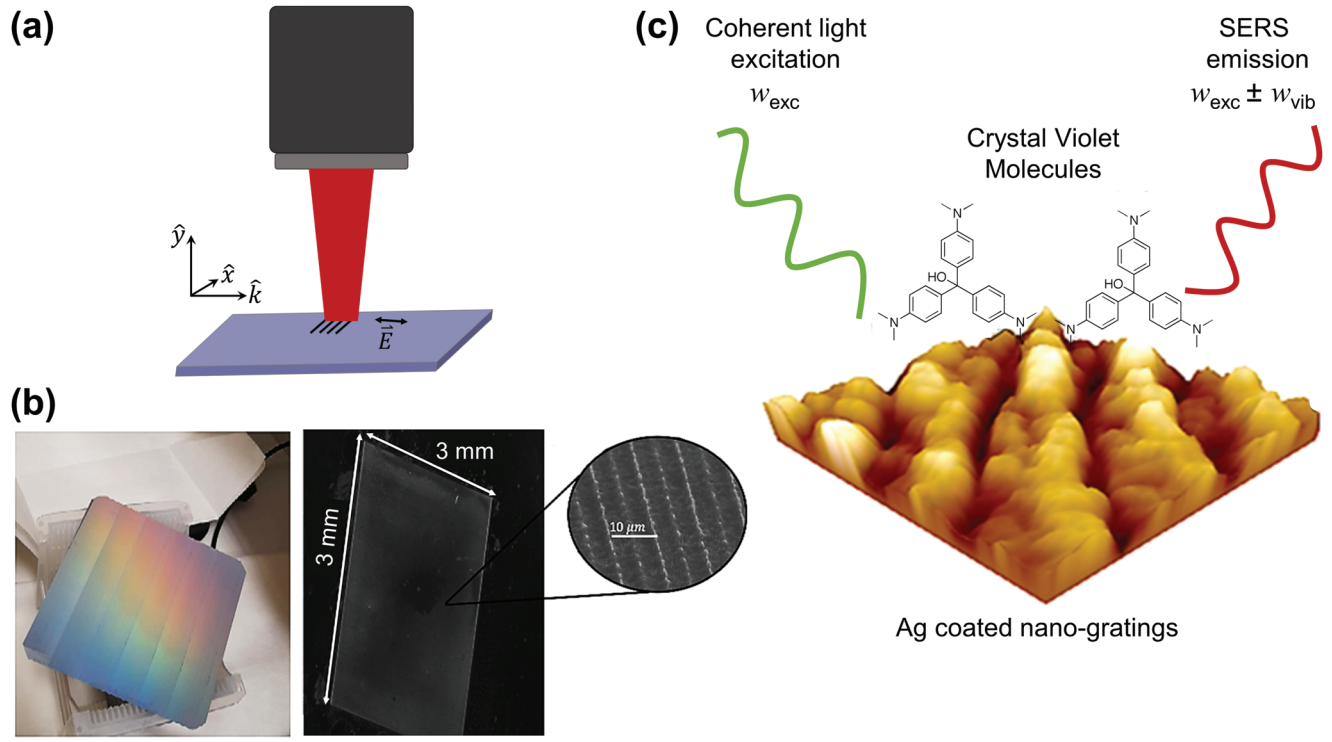

Figure 1. a) Direct laser writing technique to form nanoripples on surface b) Si-LSFL substrate fabricated by femtosecond laser (λ = 1030 nm, 370 fs pulse duration, 1 MHz repetition rate) on a full 6" × 6" Si wafer and Si-HSFL substrate with 3 mm × 3 mm dimensions fabricated by femtosecond laser (λ = 1550 nm, 450 fs pulse duration, 1 MHz repetition rate) on polished Si wafer surface. c) Schematic illustration of the SERS measurement over 3D AFM image of a LIPSS pattern.

permittivity of the material turns into the metallic state and triggers the Surface Plasmon Polariton (SPP) propagation on the surface.[48–50] However, Sipe theory does not cover any feedback mechanism of multiple pulse operations which is required for obtaining HSFL structures. Until recent years, HSFL structures were mainly processed on the surface of bulk metals and semiconductors. In addition to the surface structuring, switching the wavelength to a region, transparent for the material, provides a 3D and also subsurface HSFL generation under the substrates.[27,51,52] A recent study attempting to explain HSFL structures was by Li Z. et al. in 2021.[46] It was demonstrated that the competition between penetration loss of femtosecond laser pulse and propagation loss determines the period of the HSFL structures. Peak excitation efficiency of sub-SPPs controls the stability of HSFL periods.

In this study, we demonstrate that self-organized, quasi-periodic LIPSS structures can embody the required randomness and roughness to accommodate a high hotspot density to act as sensitive SERS substrates with performance comparable to well-established top-down approaches. We present and compare the quasi-periodic structures on the silicon (Si) surface in two different structuring regimes, namely LSFL and HSFL. We show that by simple metal coating of LIPSS patterned Si substrates, we can convert them to robust and high EF exhibiting nanoplasmonic SERS substrates. LIPSS-based SERS substrates exhibit EFs at an order of 10^9 which is a ballpark figure of performance comparable to that of chemically synthesized nanostructures such as nanoplates, nanowires, and nanoparticles.[53–55] Control of the processed region is also accurate and flexible. **Figure 1** shows the overview of the fabrication and analysis processes of Si-HSFL and Si-LSFL substrates.

2. Results & Discussion

2.1. Sample Characterizations

HSFL structures are produced on polished Si surfaces by direct laser writing technique using a 3-axis motorized stage and a homemade fiber laser[56] operating at 1550 nm wavelength, ≈450 fs pulse duration, ≈1 μJ maximum pulse energy, and 1 MHz repetition rate. The LFSL structures are produced on a polished Si surface by direct laser writing technique using a 2-axis galvo-scanner and a homemade fiber laser[57] operating at 1032 nm wavelength, ≈370 fs pulse duration, ≈1 μJ maximum pulse energy, and 1 MHz repetition rate. In both HSFL and LSFL cases, the LIPSS structures are formed continuously over ≈cm^2 large areas with an orientation perpendicular to the laser polarization direction with periodicities of 290 and 890 nm, respectively. In both cases, Si orientation, doping type, doping level, or conductivity are found not to have significant effects on the results from undoped up to moderate doping levels.

2.1.1. Si-HSFL Structures

The results presented in **Figure 2**a,b, represent size and shape variation of Si-HSFL structure and after 30 nm silver

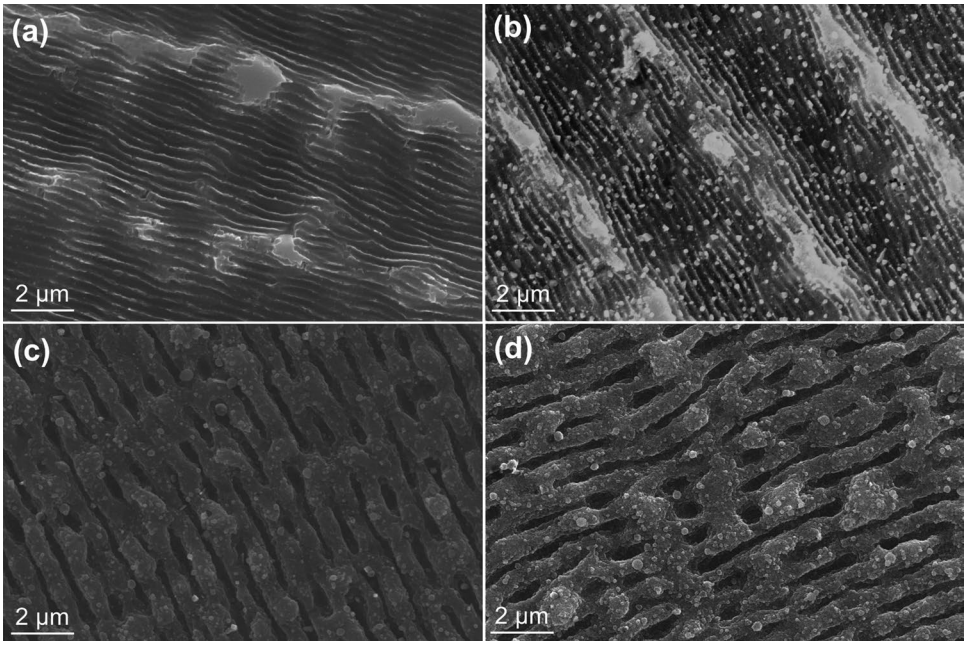

Figure 2. SEM images of a) Si-HSFL, b) 30 nm Ag and 10^{-5} M CV coated Si-HSFL, c) Si-LSFL, and d) 30 nm Ag and 10^{-5} M CV coated Si-LSFL structures. Scale bar is 2 μm.

(Ag) and 10^{-5} M crystal violet[58] (CV) deposition, respectively. Two types of periodicities are introduced. By calculating 2D Fast Fourier Transform (FFT) of the structures, smaller periodicity of the features is determined as 290 nm. Average depth calculated from atomic force microscopy (AFM) cross sections of the features is 105 nm. Sub-surface plasmon polaritons (sub-SPPs) generated at the subsurface of the materials have been suggested to explain the formation of HSFL structures.[46] Li Z. et al. demonstrated that competition between penetration loss of femtosecond laser pulse and propagation loss determined the period of the HSFL structures. Peak excitation efficiency of sub-SPPs controls the stability of HSFL periods.

2.1.2. Si-LSFL Structures

The results presented in Figure 2c,d, represent size and shape variation of Si-LSFL structure before and after 30 nm Ag and 10^{-5} M CV deposition, respectively. Apart from multi-pulse feedback phenomena, LSFL periodicity is directly related to the SPP wavelength.[59] For this type of LSFL formation, periods of the structure are not significantly different from irradiation wavelength. By calculating 2D-FFT of the structures, periodicity of the features is determined as 890 nm and the average depth, measured by AFM, is 390 nm.

2.2. Raman Enhancement for the Si-HSFL and Si-LSFL Structures

Figure 3 shows EF statistics of 10^{-5} M CV coated HSFL (solid lines) and LSFL (dotted lines) substrates with varying Ag thickness for 532 (a, b), 660 (c, d), and 785 nm (e, f) Raman excitation wavelengths, respectively. Detailed calculation of surface averaged EF values can be found in Section 2.3.

To obtain the largest local field enhancement without losing the obtained nanoscale surface area, thickness of Ag is optimized for Si-HSFL and Si-LSFL substrates at different Raman excitation wavelengths.

To preserve the same thin film property on each SERS substrate the vacuum pressure, deposition rate, deposition angle, and chamber temperature are kept constant. When the Ag deposition on the SERS substrates forms separate globular clusters rather than uniform thin film, the source of the SERS activity is determined as individual nanoclusters.[60,61] In such a case, the effect of the Ag thickness on the SERS substrates cannot be determined. In this study, the threshold for a uniform Ag thin film for the Si-HSFL and Si-LSFL SERS substrates is determined as 40 nm. SERS performance of the 40 nm Ag coated Si-HSFL structures decreased with the increased Raman excitation wavelength, but 50 and 70 nm Ag coated Si-HSFL structures exhibited a behavior in which the optimal Raman excitation wavelength is 660 nm. For a SERS substrate under laser excitation wavelength 532 nm, optimized Ag thickness is determined as 50 nm for Si-HSFL and 70 nm for Si-LSFL. SERS performance of the 50 and 70 nm Ag coated Si-HSFL structures present competing results. Simultaneous optimization of both Raman intensity and cost efficiency of the SERS substrate highlights a 50 nm optimal Ag thickness. The highest intensity of all SERS substrates is demonstrated for 660 nm excitation wavelength. 70 nm Ag coated Si-LSFL structures perform the highest intensity for 532, 660, and 785 nm Raman excitation wavelengths. Further discussion on optimal paramecan be found in the Supporting Information Section 1, Figures S1–S3.

SERS spectra of the 10^{-5} – 10^{-11} M CV under the irradiation of 532 and 660 nm laser on Si-HSFL structures are shown in **Figure 4**a,b. The four main characteristic SERS peaks of CV

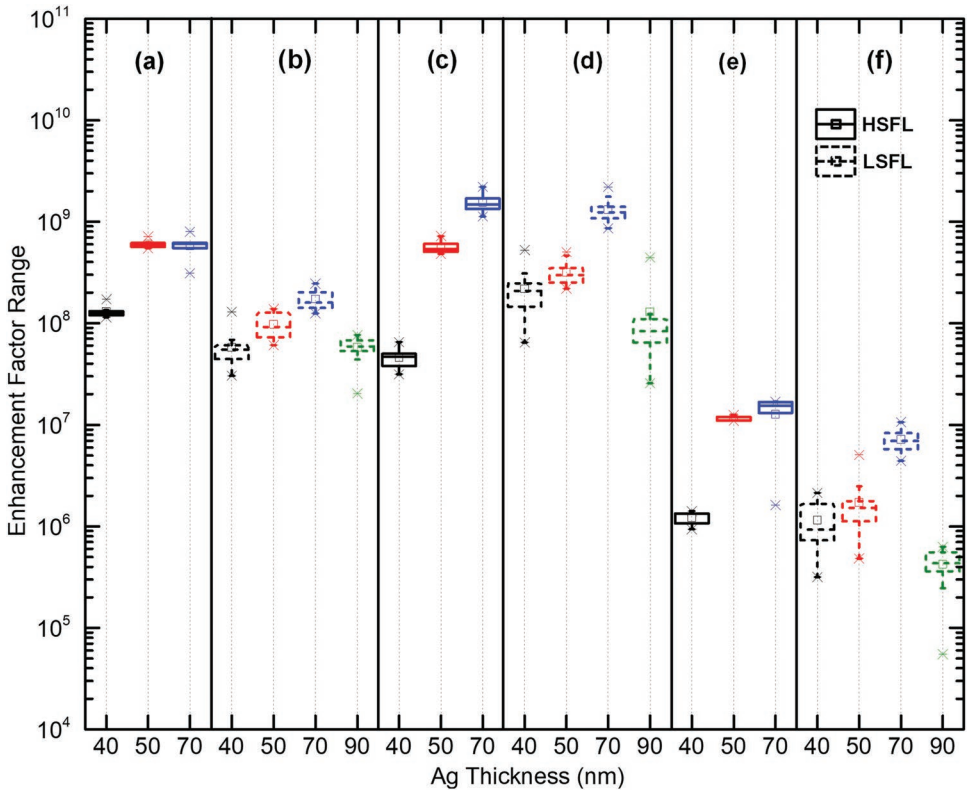

Figure 3. Box charts displaying the population statistics of EFs of Si-HSFL structures (solid lines) for a) 532, c) 660, and e) 785 nm Raman excitation wavelengths and Si-LSFL structures (dotted lines) for b) 532, d) 660, and f) 785 nm Raman excitation wavelengths with varying Ag thickness. (1371 cm^{-1} assigned to the N-phenyl stretching band of CV at 1374 cm^{-1} for EF calculations).

on our 50 nm Ag coated Si-HSFL substrates are observed for the low CV concentration measurements at 532 nm excitation wavelength. Band assignments of these modes are listed as 940 cm^{-1} ring skeletal vibrations, 1295 cm^{-1} ring C—C stretching, 1374 cm^{-1} N-phenyl stretching, and 1615 cm^{-1} C—C stretching. During the low CV concentration measurements of 50 nm Ag coated Si-HSFL structures at 660 nm excitation wavelength, additional characteristic SERS peaks of CV are observed at 716 and 750 cm^{-1}. Complete set of band assignments of CV molecule is listed as 348 cm^{-1} C^{+}-phenyl bending, 434 cm^{-1} out of plane ring C—C bending, 528 cm^{-1} ring skeletal vibration of radical orientation, 732 and 760 cm^{-1} out of plane C—H bending, 815 cm^{-1} out of plane ring C—H bending, 1586 cm^{-1} ring C—C stretching, 1177 cm^{-1} in plane ring C—H

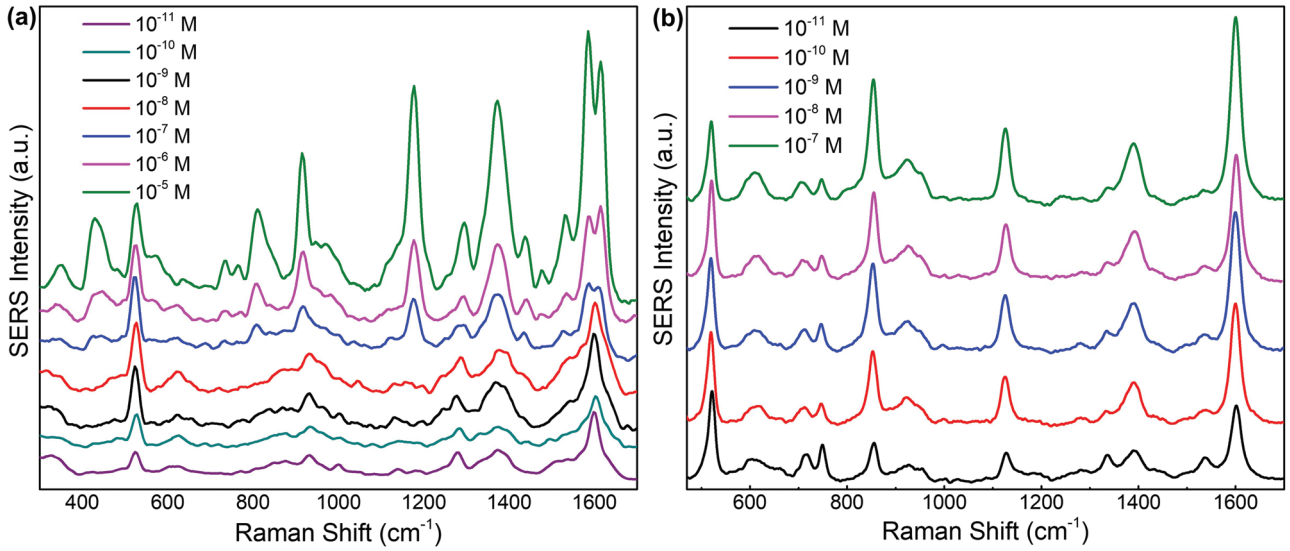

Figure 4. Raman spectra acquired from different concentrations of CV on 50 nm Ag coated Si-HSFL substrates excited at a) 532 and b) 660 nm.

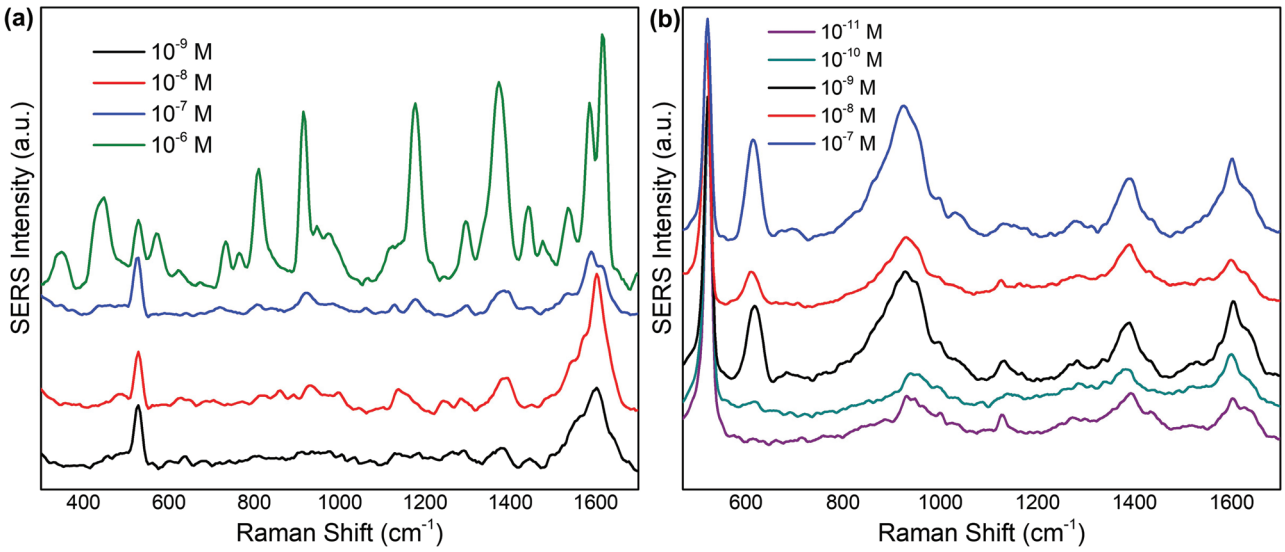

Figure 5. Raman spectra acquired from different concentrations of CV on a 70 nm Ag coated Si-LSFL substrate excited at a) 532 and b) 660 nm.

bending, 1535 cm^{-1} ring C—C stretching, and 1446 cm^{-1} ring C—C stretching + ring deformation.[58,62]

When the Raman enhancement results are evaluated, it is found that the Si-HSFL SERS substrate exhibits a lower limit of detection (LoD) for 660 nm Raman excitation wavelength. Since the SERS mechanism of direct laser written structures is directly affected by the tightening of the nanoripples, hotspot density of Si-LSFL structures is lower than Si-HSFL structures. SERS spectra of the 10^{-6} – 10^{-9} and 10^{-7} – 10^{-11} M CV under the irradiation of 532 and 660 nm laser on 70 nm Ag Si-LSFL structures are shown in **Figure 5**a,b.

The results of the Raman intensity versus CV concentration study performed for the determination of LoDs for Si-HSFL and Si-LSFL substrates are presented in **Figure 6**.

Characteristic SERS peak of a CV molecule at 1374 cm^{-1}, is detected down to 10^{-11} M for Si-HSFL and 10^{-10} M for Si-LSFL structures with a good signal-to-noise ratio at 532 nm excitation wavelength. Corresponding LoDs of the Si-LSFL and Si-HSFL structures under the irradiation of 532 nm are determined to be as low as 10^{-11} and 10^{-10} M, respectively, as shown in Figure 6a. For the 660 nm Raman excitation wavelength, peak at 1374 cm^{-1} is detected down to 10^{-11} M for both types of the SERS substrates. Corresponding LoDs of the Si-LSFL and Si-HSFL structures for the irradiation of 660 nm are determined to be as low as 10^{-11} as shown in Figure 6b. Both x and y-axis are demonstrated in the logarithmic scale.

2.3. Uniformity of Si-LSFL and Si-HSFL SERS Substrates

Another aspect that needs attention in SERS substrate fabrication is uniformity. The uniformity of the SERS activity for 50 nm Ag deposited Si-HSFL substrates and 70 nm Ag deposited Si-LSFL substrates has been investigated by Raman mapping.

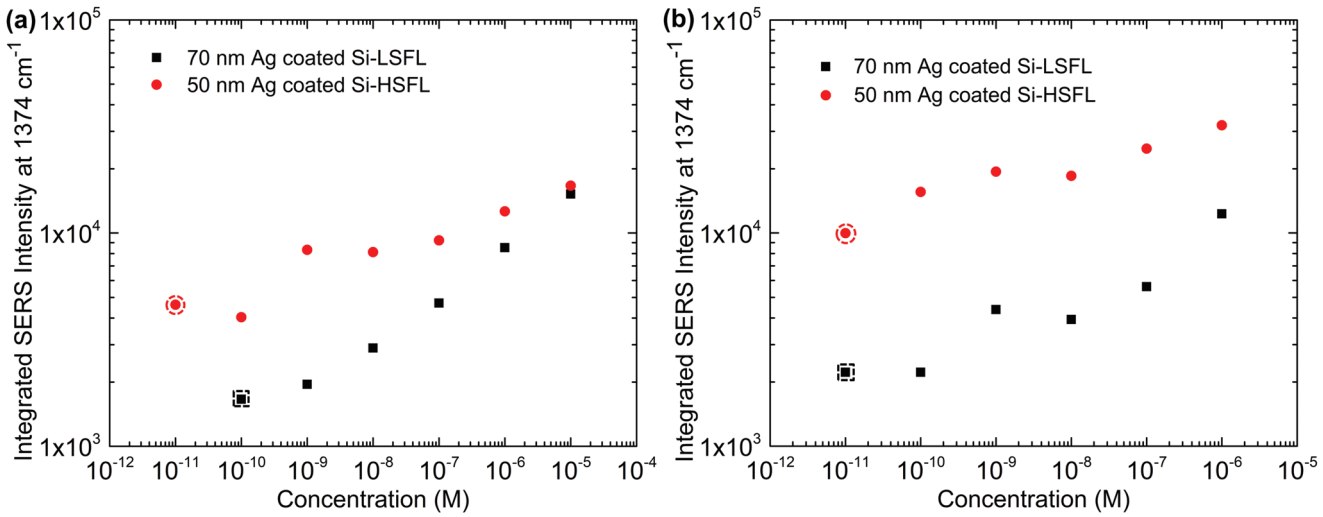

Figure 6. SERS intensity curves of 50 nm Ag coated Si-HSFL and 70 nm Ag coated Si-LSFL structure at different CV concentrations for the determination of corresponding LoDs obtained for a) 532 and b) 660 nm Raman excitation wavelengths.

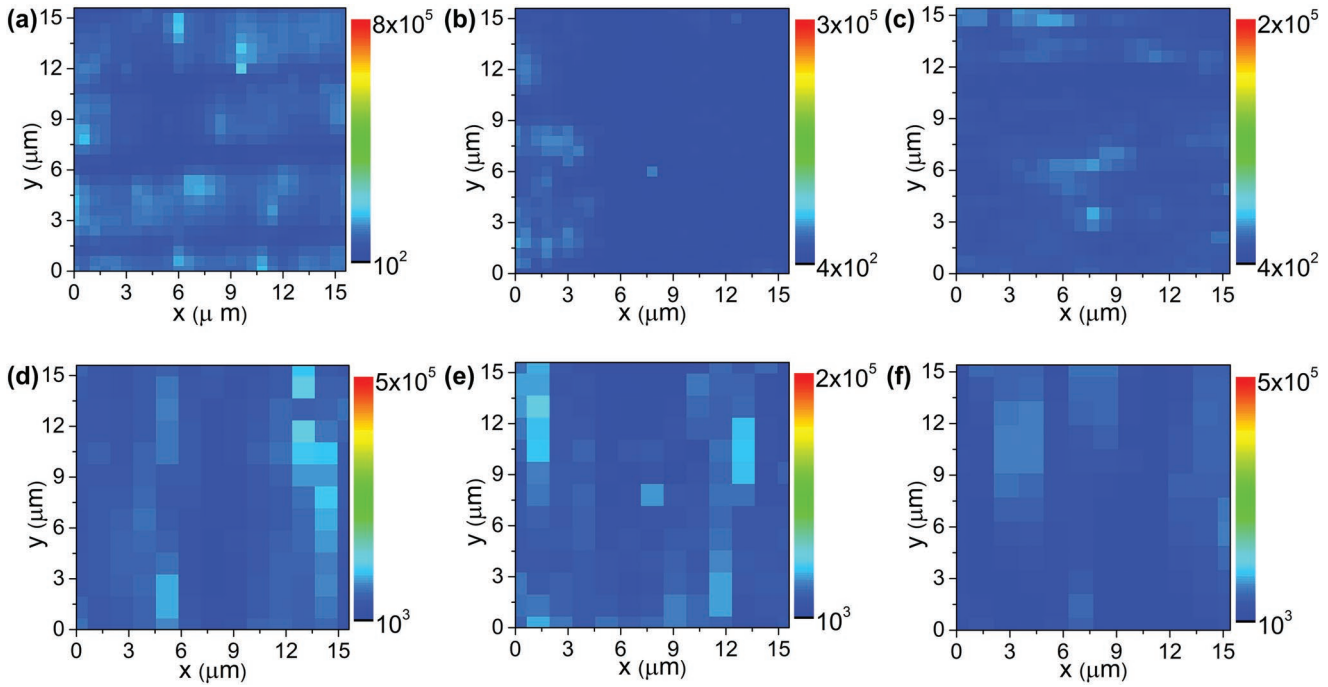

Figure 7. Raman map of 10^{-5} M CV coated on 50 nm Ag deposited Si-HSFL substrates acquired with a) 532, b) 633, and c) 785 nm excitation wavelengths and 70 nm Ag deposited Si-LSFL substrates acquired with d) 532, e) 633, and f) 785 nm excitation wavelengths.

Raman map measurements are performed with 532, 633, and 785 nm excitation wavelengths (Renishaw/In Via). After baseline correction of the Raw Raman map data, I_{SERS} for each pixel is calculated through the area under the peak 1371 cm^{-1} with a width between 1319 and 1421 cm^{-1}. **Figure 7** shows ±27% and ±24% average SERS signal variation for Si-HSFL and Si-LSFL substrates over a 2.40×10^{-4} mm^2 area, respectively.

Figure 8 shows SERS signal profiles of corresponding horizontal pixels on Raman maps of 50 nm Ag deposited Si-HSFL substrate (Figure 7a) and 70 nm Ag deposited Si-LSFL substrate (Figure 7d) acquired with 532 nm Raman excitation

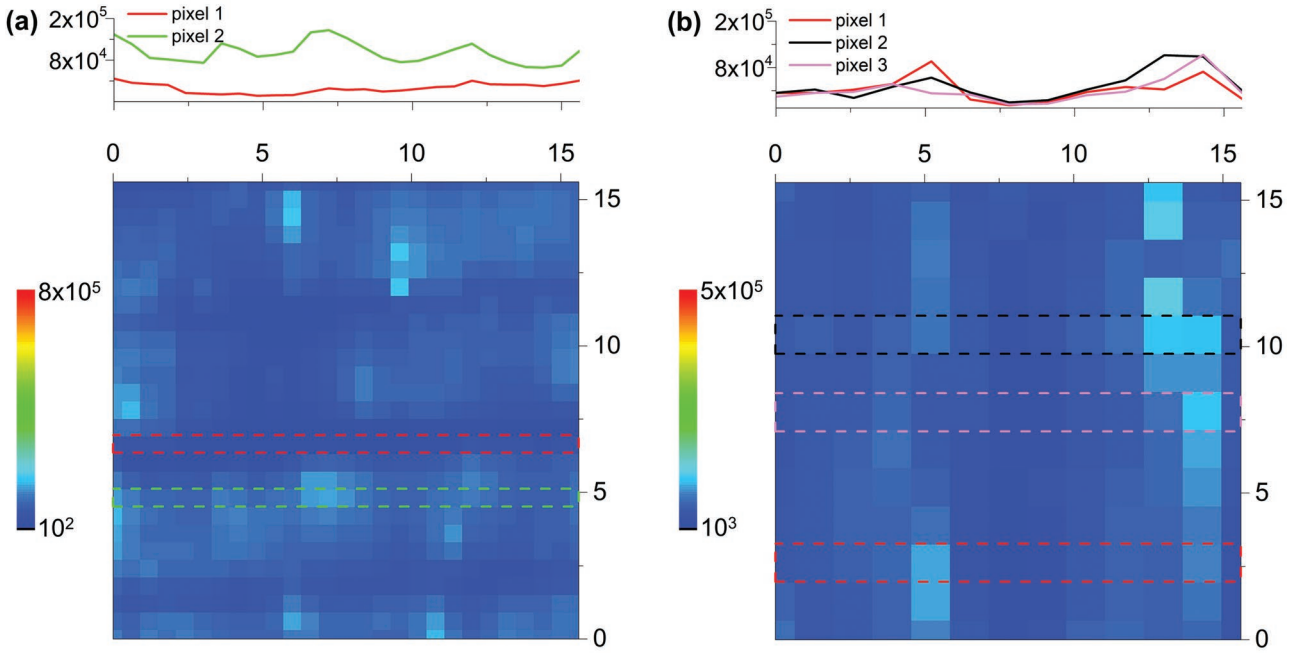

Figure 8. SERS signal profiles of shown pixels on Raman maps of a) 10^{-5} M CV coated on 50 nm Ag deposited Si-HSFL substrates and b) 70 nm Ag deposited Si-LSFL substrates acquired with 532 nm Raman excitation wavelength.

wavelength. In Figure 8a, pixel 1 (red) represents the 290 nm periodic area revealing ±15% average SERS signal variation and pixel 2 (green) includes the hatch center together with 290 nm periodicity revealing ±35% SERS signal variation. Figure 8b indicates a similar signal profile for the randomly chosen three pixels and ±29% signal variation all over the surface. In Figure 7 and Figure 8, the 5 µm hatch distance of processed HSFL substrates can also be identified with the mapping results.

2.4. Field Enhancement

All Raman measurements are conducted using 100×/0.90 NA objective, 17, 21, and 25 µm spot sizes for 532, 660, and 785 nm, respectively, and 6.4 mW power laser power but integration time is optimized from sample to sample in order to increase the signal to noise ratio and avoid sample damaging. In normal Raman spectroscopy (NRS) inside liquid samples, the 3D Raman probe volume can be determined by considering a prolate spheroid focal volume, which in our 532 nm excitation source case has dimensions of r_x = 8.5 µm, r_y = 8.5 µm, and r_z (depth of focus) = 17 µm, yielding $V_{probe} = (4\pi/3) \times 8.5\ \mu m \times 8.5\ \mu m \times 17\ \mu m \cong 5 \times 10^{-12}$ L of probe volume. For our 10^{-2} M CV solution, the total number of molecules ($N_{NRS} = C_{NRS} \times V_{probe}$) in the measurement volume can be found as $N_{NRS} = 10^{-2}$ mol $L^{-1} \times 6.02 \times 10^{23}$ molecules $mol^{-1} \times 5 \times 10^{-12}$ L $\cong 3 \times 10^{10}$ molecules. The raw spectral data are normalized with respect to integration time. After baseline correction, I_{NRS} is calculated through the area under the peak (1371 cm^{-1} corresponding to the N-phenyl stretching band at 1374 cm^{-1}) with a width between 1319 and 1421 cm^{-1} and is found as 2500 cts s^{-1} for 532 nm, 2190 cts s^{-1} for 660 nm, and 1990 cts s^{-1} for 785 nm. Surface area of the Si-HSFL and Si-LSFL substrates obtained from 10 µm × 10 µm area of AFM images is determined to be 322.8 and 328.0 μm^2 by proportion, respectively. Molecules in near field span up to 2 nm from the surface of the metal film, resulting in a probe volume of $V_{probe\text{-}HSFL} = 322.8\ \mu m^2 \times 0.002\ \mu m \cong 6 \times 10^{-16}$ L and $V_{probe\text{-}LSFL} = 328.0\ \mu m^2 \times 0.002\ \mu m \cong 7 \times 10^{-16}$ L. Therefore, the total number of CV molecules in the SERS measurement can be calculated as $N_{SERS\text{-}HSFL} = 10^{-5}$ mol $L^{-1} \times 6.02 \times 10^{23}$ molecules $mol^{-1} \times 6 \times 10^{-16}$ L = 3.9×10^3 molecules and $N_{SERS\text{-}LSFL} = 10^{-5}$ mol $L^{-1} \times 6.02 \times 10^{23}$ molecules $mol^{-1} \times 7 \times 10^{-16}$ L = 4.2×10^3 molecules. For 660 nm excitation wavelength, $N_{NRS} \cong 5.8 \times 10^{10}$ molecules and $N_{SERS\text{-}HSFL} = 5.9 \times 10^3$ molecules, $N_{SERS\text{-}LSFL} = 6.0 \times 10^3$ molecules. For 785 nm excitation wavelength, $N_{NRS} \cong 9.6 \times 10^{10}$ molecules and $N_{SERS\text{-}HSFL} = 8.4 \times 10^3$ molecules, $N_{SERS\text{-}LSFL} = 8.5 \times 10^3$ molecules. Surface averaged SERS EF is calculated with the measured I_{NRS} and I_{SERS} values as $EF = (I_{SERS}/N_{SERS}) \times (N_{NRS}/I_{NRS})$. EF values of 70 nm Ag deposited HSFL substrates are 5.8×10^8, 1.9×10^9, 1.8×10^7, and for 70 nm Ag deposited LSFL substrates are 1.7×10^8, 1.6×10^9, 1.0×10^7 for 532, 660, and 785 nm excitation wavelengths, respectively.

Another approach for EF calculation may be to assume that the entire substrate surface is covered with a monolayer of the molecule independent of the original analyte concentration due to good adsorption of the molecule to the substrate surface. Using this approach, of course, one would calculate much less EFs due to high N_{SERS} in the maximally populated scenario. It should, however, be pointed out that SERS is found to originate from highly localized regions called hot-spots, which do not make up more than about 0.01% of the substrate area.[63] Therefore, whatever the EF is calculated from the dense population scenario, the actual number of molecules that contribute to the SERS signal make up about only 1 part in 10^4 of the N_{SERS} calculated this way. The reported cross-sectional areas of a CV molecule are 0.4 nm^2 and 4 nm^2, representing perpendicular and parallel orientations of the adsorbed CV molecule on the substrate surface, respectively.[64] Surface areas of the Si-HSFL and Si-LSFL substrates are 323 and ≈ 328 μm^2, respectively. $N_{adsorbed\text{-}HSFL\text{-}perp.} = 323 \times 10^6\ nm^2/0.4\ nm^2\ 8.1 \times 10^8$ molecules assuming perpendicular orientation of adsorbed CV. $N_{adsorbed\text{-}HSFL\text{-}par.} = 323 \times 10^6\ nm^2/4\ nm^2\ 8.1 \times 10^7$ molecules assuming parallel orientation of the adsorbed CV. $N_{adsorbed\text{-}LSFL\text{-}perp.} = 328 \times 10^6\ nm^2/0.4\ nm^2\ 8.2 \times 10^8$ molecules for perpendicular orientation. $N_{adsorbed\text{-}LSFL\text{-}par.} = 328 \times 10^6\ nm^2/4\ nm^2\ 8.2 \times 10^7$ molecules for parallel orientation. N_{NRS} and I_{NRS} are calculated the same as in the previous approach ($N_{NRS} = 10^{-2}$ mol $L^{-1} \times 6.02 \times 10^{23}$ molecules $mol^{-1} \times 5.14 \times 10^{-12}$ L = 3.09×10^{10} molecules. After baseline correction, I_{NRS} is calculated through the area under the peak 1371 cm^{-1} with a width between 1319 and 1421 cm^{-1} and is found as 2500 cts s^{-1} for 532 nm and 2190 cts s^{-1} for 660 nm). For the 70 nm Ag coated Si-HSFL structures at 660 nm laser excitation, the obtained N_{SERS} and N_{NRS} values accordingly lead to $EF = (I_{SERS}/N_{adsorbed}) \times (N_{NRS}/I_{NRS}) = (424818/8.1 \times 10^7) \times (3.09 \times 10^{10}/2190) \cong 7.4 \times 10^4$ assuming parallel and 7.4×10^3 assuming perpendicular orientations of CV molecule. Incorporating the 10^4 factor as indicated by Kneipp, et al. for the sparsity of the hotspots, one arrives at an estimated EF range of 10^8–10^9, a range not very different from that of the previous approach.

Quantitative determination of chemical enhancement is a challenging problem because SERS spectra contain both electromagnetic and chemical contributions. The finite-elements method (FEM) based Maxwell solver that we used for the expected EF values includes a near-field scattered field without computing metal-molecule interaction. However, the difference between the experimental and simulation-based EF values may be the way to indirectly detect the chemical enhancement. In our recent study, we showed that most enhanced Raman signals are observed from the substrates with dense etched surfaces and no significant signal is obtained from Ag on flat Si surfaces.[65]

2.5. Raman Enhancement Factor Simulations

In order to compare the experimental results to expected EFs from LSFL and HSFL structures, we have performed FEM-based Maxwell solver simulations using COMSOL Multiphysics.[66] Since faithful representations of the Si-LSFL and Si-HSFL structures are aimed, scanning electron microscope (SEM) images of the nanoripples are used in the simulations. Apart from the edge smoothings, the images are not post-processed. 3D maps of EF for 50 nm Ag coated HSFL, 70 nm Ag coated LSFL structures and corresponding SEM images are shown in **Figure 9**. The maximum of the colormap is chosen as 14 in the logarithmic scale of Raman EF so that the regions where enhancement is stronger are clearly apparent. The

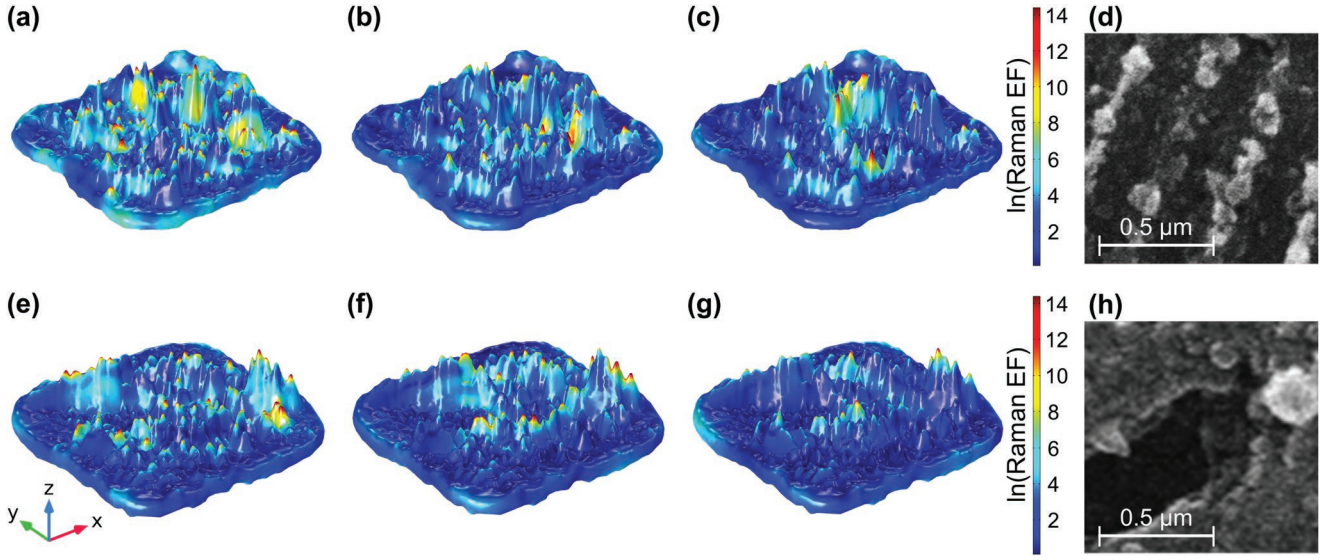

Figure 9. EF calculated for 50 nm Ag coated HSFL structure at a) 532, b) 660, and c) 785 nm, d) SEM image of HSFL structure used for simulations, and EF calculated for 70 nm Ag coated LSFL structure at e) 532, f) 660, and g) 785 nm (logarithmic color scale- $\log_e$ (Raman EF), h) SEM image of LSFL structure used for simulations.

arbitrarily chosen regions from SEM images of HSFL and LSFL structures with 1.0 μm × 1.0 μm areas used for FEM simulations are presented in **Figure 10**d,h.

Please note that the Raman EF is approximately field EF[4].

$$|E(\lambda_{\text{excitation}})|^2 \times |E(\lambda_{\text{Raman}})|^2 \cong |E(\lambda_{\text{excitation}})|^4 \quad (1)$$

EF values calculated from the simulation are 5.3×10^{13}, 3.0×10^{13}, and 3.5×10^{13} for 50 nm Ag deposited HSFL substrates, and 1.6×10^{11}, 1.8×10^{12}, and 5.4×10^{9} for 70 nm Ag deposited LSFL substrates at 532, 660, and 785 nm excitation wavelengths

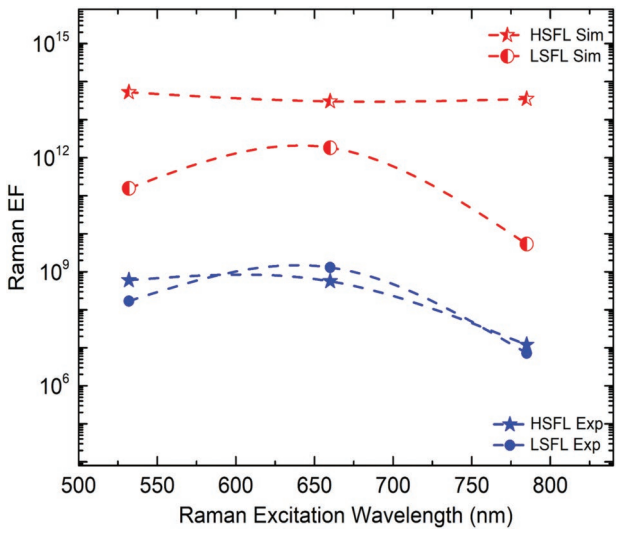

Figure 10. Raman EFs at 532, 660, and 785 nm Raman excitation wavelengths as determined by experiment (blue solid symbols), simulation (red semi-solid symbols) of 50 nm Ag coated HSFL and 70 nm Ag coated LSFL structure. Dashed lines are spline fits to all data and are presented only to guide the eye and simulation results belong to the average of 0°, 45°, and 90° incidence polarization angles).

for the average of 0°, 45°, and 90° incidence polarization angles. Experimentally determined EF values of 50 nm Ag deposited HSFL substrates are 6.0×10^8, 6.9×10^8, 1.7×10^7, and 70 nm Ag deposited LSFL substrates are 1.7×10^8, 1.6×10^9, and 1.0×10^7 for 532, 660, and 785 nm excitation wavelengths. Field enhancement through inter-particle plasmon coupling has been presented by closely packed multi-spiked gold nanoparticles.[67] Tightened interparticle spacing of the multi-spiked gold nanoparticles generates interparticle plasmon coupling which leads to increased hot spot density. Similarly, in addition to the spike points of the structures, highly localized regions of the intense field enhancement are presented at the nanogaps between features of Si-HSFL and Si-LSFL at 660 nm Raman excitation wavelength.

An overview of EFs determined experimentally, from FEM simulations, is displayed in Figure 10. Simulation results represent Raman EF of the HSFL and LSFL structures for an average of 0°, 45°, and 90° incidence polarization angles at different wavelengths.

It is noticeable that the EFs determined from two different approaches display similar trends where the magnitudes do not agree. This is because the FEM simulations possible in practical durations cannot cover extensive areas as in the experiment and they merely under-represent the actual surface. We would like to note that the maximum experimental EF value is obtained for 70 nm Ag deposited HSFL substrate as 1.9×10^9, and for 70 nm Ag deposited LSFL substrate as 1.6×10^9 acquired with 660 nm excitation wavelength. Expected EFs from simulations confirm the experimental results such that the enhancement performance of HSFL structures is at least an order of magnitude higher than that of the LSFL structures. Computed polarization angle dependence of the EF values of 50 nm Ag coated Si-HSFL and 70 nm Ag coated Si-LSFL structures at excitation wavelengths of 532, 660, and 785 nm are shown in **Figure 11**. Excitation wavelength dependence of the 70 nm Ag coated Si-LSFL structures presents higher order of magnitude differences

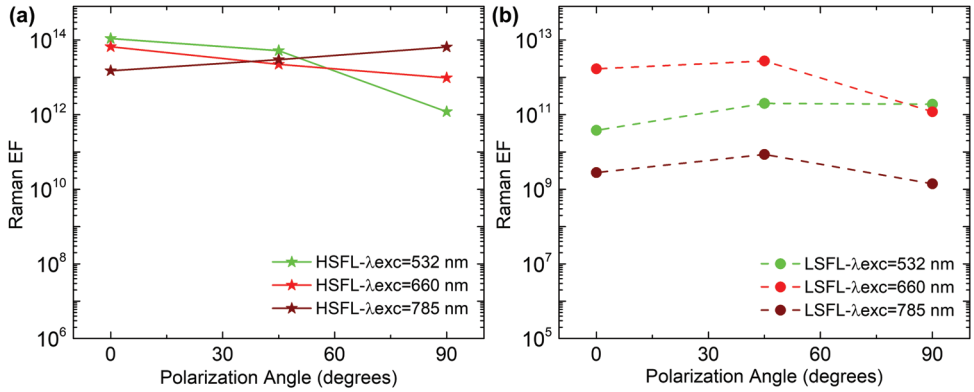

Figure 11. Raman EF calculated for a) 50 nm Ag coated HSFL, and b) 70 nm Ag coated LSFL structures with different incidence polarization angles at 532, 660, and 785 nm.

relative to the Si-HSFL structures. In contrast, polarization angle dependence is lower for 70 nm Ag coated Si-LSFL structure, relative to the 50 nm Ag coated Si-HSFL structure.

3. Conclusion

A novel method is proposed to produce SERS substrates using two different structuring regimes of LIPSS, which has a profound effect on localized electric field enhancement. Fast fabrication of highly sensitive SERS substrates in large areas with high uniformity is achieved for both Si-HSFL and Si-LSFL structures. Population statistics of SERS signals are presented for two different regimes of LIPPS comparatively by determining the optimum metal thin film layer and proper excitation wavelength. The maximum experimental EF values are obtained for 70 nm Ag deposited HSFL and LSFL substrates as 1.9×10^9 and 1.6×10^9, respectively, acquired with 660 nm excitation wavelength. Higher number of characteristic CV peaks are identified for low CV concentration measurements of Si-HSFL structures at 660 nm excitation wavelength. LoD for the CV molecule is demonstrated as 10^{-11} M for both Si-HSFL and Si-LSFL structures at 660 nm Raman excitation wavelength. For the 532 nm Raman excitation wavelength, LoD of the CV molecule is demonstrated as 10^{-11} M for Si-HSFL and 10^{-10} M for Si-LSFL structures. The uniformity of the SERS signal has been investigated by Raman mapping revealing ±27% and ±24% deviation for Si-HSFL and Si-LSFL substrates over a 2.40×10^{-4} mm^2 area, respectively. Therefore, metal-coated LIPSS Si fabricated by fs laser with excellent spatial selectivity and uniformity can be used as efficient SERS substrates. Furthermore, uniform EF calculation results in between and show that this low-cost, fast and efficient SERS substrate preparation method has great potential for trace amounts of analyte detection.

4. Experimental Section

LIPSS on Si: Two different house-made fs laser processing systems were used to produce LSFL and HSFL LIPSS structures as detailed in the next sections.

Formation of Si-HSFL Structures: HSFL structures were manufactured using ultrafast laser on n-type Si <100> wafer substrate. The substrate was exposed to 1550 nm laser irradiation, having 450 fs pulse duration and 1 MHz repetition rate. The photon energy of the laser was ≈0.71 eV and the bandgap of the Si was 1.11 eV at 300 K. To process Si with 1550 nm laser irradiation, it was required to trigger a two-photon absorption (TPA) mechanism. Thus, the fluence on the processed region was adjusted to ≈2600 J cm^{-2} which was corresponding to 2500 pulses on the spot area. To reach desired fluency level, a high NA = 0.45 aspheric lens with a focal length of 8 mm was used. Three-axis motorized stages were used to perform raster scanning and the dimension of the sample was set to 1 mm × 3 mm with a hatch distance of 5 µm. The repeatability of the process mainly depends on the focal depth. Rayleigh length of the focusing beam in the HSFL setup was ≈1/10 times smaller than for the LSFL setup.[68] Unlike LSFL fabrication, the HSFL structures did not form directly on the surface (**Figure 12**), but were formed as

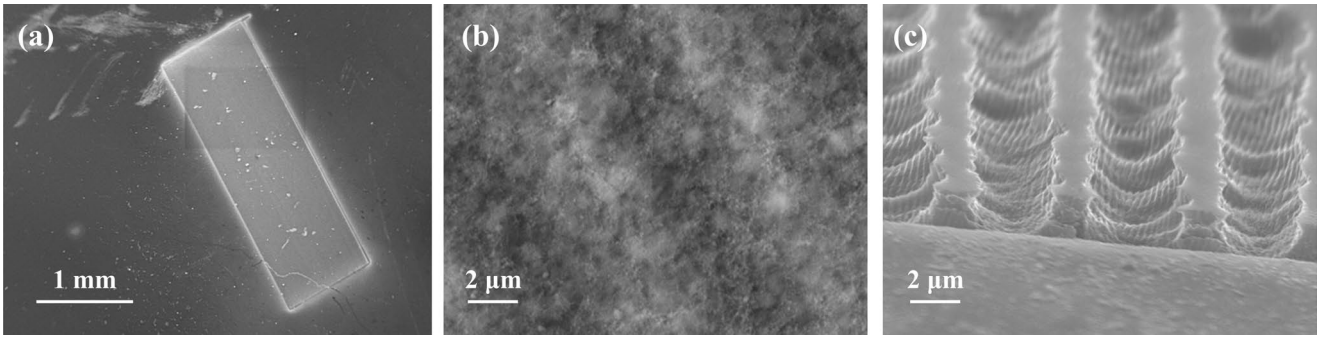

Figure 12. SEM images of a) HSFL structured area, b) the polymorphic Si surface before selective etching, and c) 70-degree view of the c-Si after the etching.

subsurface structures right below the surface. It was required to remove the capping polycrystalline Si layer above the HSFL structure created by melting and recrystallization during laser processing by a dedicated specially designed selective etchant.[51,52] The HSFL structures were created perpendicular to the polarization direction of the beam.

Formation of Si-LSFL Structures: For the silicon (Si) structuring, n-type Si <100> wafer (Czochralski, double-side polish, 275 µm, 1–3 Ω cm) was used as the substrate. All Si wafers were cleaned in a piranha solution, 1:3 ratio of hydrogen peroxide (H_2O_2, Merck, 30%) and sulfuric acid (H_2SO_4, Merck, 95–97%) at 75 °C for 15 min. After rinsing in deionized (DI) water, they were cleaned in an RCA solution, 1:1:5 ratio of H_2O_2, hydrochloric acid (HCl, Merck, 37%), and water (H_2O), at 75 °C for 15 min. Last, Si wafers were rinsed in DI water and dried by N_2 blowing.

Generation of LIPSS was achieved by a femtosecond laser operating at a central wavelength of 1030 nm with pulse duration 370 fs, repetition rate 1 MHz, and spot size 16 µm. Periodic nanostructures were obtained in a 5 mm × 5 mm area using a galvo-scanner.[68] Influential parameters in creating these structures were pulse energy, pulse density, and polarization direction of light in terms of scanning lines. Line distance/hatch of 7 µm, with processing speeds of 3, 5, 7, and 10 m s^{-1} were tested, which was equal to the average number of 19.0, 11.5, 8.2, and 5.7 pulses per focal spot, respectively. Pulse energy for the formation of Si-LSFL structures was 1.2 µJ, with the laser fluence 0.557 J cm^{-2}. The polarization was 45° with respect to scanning lines. The detailed description of the laser scanning setup can be found in a previous publication of one of the authors.[68]

Silver Deposition: Ag layers with thicknesses 30, 40, 50, 70, and 90 nm were thermally evaporated onto Si-LSFL, and Si-HSFL structures in a box-coater system with a vacuum base pressure less than 5×10^{-6} Torr and at a deposition rate of 1.2s^{-1}.

SERS Substrate Preparation: All of the SERS substrates were prepared by spin coating of 100 µL of CV ($C_{25}H_{30}ClN_3$) solution (Speciality Coating Systems G3-8). Substrates were accelerated for 5 s, spun for 30 s at 2000 rpm, and decelerated for 3 s. The Raman measurements were performed using CV purchased from Sigma-Aldrich. CV molecules with different concentrations ranging from 10^{-5} to 10^{-11} mol L^{-1} of aqueous solutions were spin-coated on the HSFL substrates. CV concentrations ranging from 10^{-5} to 10^{-10} mol L^{-1} of aqueous solutions were spin-coated on the LSFL substrates.

SEM and AFM Imaging: SEM images were used to analyze the periodicity of nano-patterns, while AFM (Veeco – MultiMode & Nanomagnetics Instruments – Ambient) images were used to investigate the depths of nano-patterns. SEM images of the substrates were collected using FEI Quanta 400F Field Emission SEM (resolution 1.2 nm). No additional sample preparation was performed before imaging the substrates.

SERS Measurements: The Raman excitation from linearly polarized continuous wave (CW) 532 (Coherent Verdi), 660 (CNI Lasers), and 785 nm (CNI Lasers) wavelength laser sources were delivered through a multimode (MM) fiber (Thorlabs) coupled (Thorlabs couplers) to an in-house modified upright microscope (Nikon Eclipse LV100) equipped with a 100X/0.90 NA objective. The excitation power was adjusted to 40 mW, resulting in 6.4 mW on the sample surface. The incident polarizations of the originally linearly polarized excitation lasers were scrambled due to MM fiber delivery. The Raman signal was collected in epi-configuration by the same objective lens and coupled into another MM fiber (Thorlabs) through a beam splitter accommodating suitable dichroic mirrors (Semrock) and notch filters (Semrock). The Raman signal was analyzed by a f/9.8, 750 mm spectrometer (Andor Shamrock SR750) with 150 l/mm grating and an EMCCD camera (Andor Newton).

Field Enhancement Simulations: COMSOL Multiphysics was used for simulating the electric field response of the SERS substrates.[66] The geometry of the structure was directly reproduced from SEM images of the LIPSS Si surfaces. Ag was assumed to accumulate in the direction parallel to the deposition direction. For both HSFL and LSFL structures, a region with a projection area of approximately 1.0 μm^2 was imported to COMSOL. The edges were smoothed using Autodesk Meshmixer to prevent artificial edge modes appearing in the simulations. Index of refraction data was taken from Johnson and Christy.[69] The structure was surrounded by perfectly matched layers and illuminated with an electromagnetic plane wave at 532, 660, and 785 nm wavelengths and at a variety of different polarizations. Maximum of the different polarizations was reported as the field enhancement and the Raman EF as unpolarized excitation was used and expected the polarization generating the maximum EF to dominate the Raman signal. Further information on modeling is provided in the Supporting Information Section 2, Figures S4 and S5.

Supporting Information

Supporting Information is available from the Wiley Online Library or from the author.

Acknowledgements

S.N.E. and F.İ. contributed equally to this work. Support from the Scientific and Technological Research Council of Turkey (TÜBİTAK) under grant nr. 119F101 was greatly acknowledged. Ö.D. thanks TÜBİTAK 2211C program. The authors thank Prof. Ahmet Oral for giving access to the Raman spectrometer and the microscope, along with METU Central Laboratory and the operators for AFM, SEM, and Raman map analysis.

Conflict of Interest

The authors declare no conflict of interest.

Data Availability Statement

The data that support the findings of this study are available from the corresponding author upon reasonable request.

Keywords

high spatial frequency LIPSS, laser-induced periodic surface structures, low spatial frequency LIPSS, surface enhanced Raman spectroscopy

Received: January 31, 2022
Revised: June 15, 2022
Published online: September 7, 2022

[1] M. Fleischmann, P. J. Hendra, A. J. McQuillan, *Chem. Phys. Lett.* **1974**, *26*,163.
[2] D. L. Jeanmaire, R. P. Van Duyne, *J. Electroanal. Chem. Interfacial Electrochem.* **1977**, *84*, 1.
[3] S. Schlücker, *Angew. Chem., Int. Ed.* **2014**, *53*, 4756.
[4] A. R. Bizzarri, S. Cannistraro, *Top. Appl. Phys.* **2006**, *103*, 279.
[5] J. Langer, D. J. de Aberasturi, J. Aizpurua, R. A. Alvarez-Puebla, B. Auguié, J. J. Baumberg, G. C. Bazan, S. E. J. Bell, A. Boisen, A. G. Brolo, J. Choo, D. Cialla-May, V. Deckert, L. Fabris, K. Faulds, F. J. García de Abajo, R. Goodacre, D. Graham, A. J. Haes, C. L. Haynes, C. Huck, T. Itoh, M. Käll, J. Kneipp, N. A. Kotov, H. Kuang, E. C. Le Ru, H. K. Lee, J. F. Li, X. Y. Ling, et al., *ACS Nano* **2020**, *14*, 28.
[6] L. Yang, Y. Peng, Y. Yang, J. Liu, H. Huang, B. Yu, J. Zhao, Y. Lu, Z. Huang, Z. Li, J. R. Lombardi, *Adv. Sci.* **2019**, *6*, 1900310.

[7] A. I. Pérez-Jiménez, D. Lyu, Z. Lu, G. Liu, B. Ren, *Chem. Sci.* **2020**, *11*, 4563.
[8] N. Chen, T. H. Xiao, Z. Luo, Y. Kitahama, K. Hiramatsu, N. Kishimoto, T. Itoh, Z. Cheng, K. Goda, *Nat. Commun.* **2020**, *11*, 4772.
[9] F. Saviñon-Flores, E. Méndez, M. López-Castaños, A. Carabarin-Lima, K. A. López-Castaños, M. A. González-Fuentes, A. Méndez-Albores, *Biosensors* **2021**, *11*, 66.
[10] J. N. Anker, W. P. Hall, O. Lyandres, N. C. Shah, J. Zhao, R. P. Van Duyne, *Nat. Mater.* **2008**, *7*, 442.
[11] D. A. Stuart, K. B. Biggs, R. P. Van Duyne, *Analyst* **2006**, *131*, 568.
[12] S. Nie, S. R. Emory, *Science* **1997**, *275*, 1102.
[13] K. Kneipp, H. Kneipp, H. G. Bohr, *Top. Appl. Phys.* **2006**, *103*, 261.
[14] R. A. Alvarez-Puebla, L. M. Liz-Marzán, *Chem. Soc. Rev.* **2012**, *41*, 43.
[15] K. Xu, R. Zhou, K. Takei, M. Hong, *Adv. Sci.* **2019**, 6.
[16] T. Vo-Dinh, F. Yan, M. B. Wabuyele, *Top. Appl. Phys.* **2006**, *426*, 409.
[17] Y. Li, K. Zhang, J. Zhao, J. Ji, C. Ji, B. Liu, *Talanta* **2016**, *147*, 493.
[18] N. K. Gushiken, G. T. Paganoto, M. L. A. Temperini, F. S. Teixeira, M. C. Salvadori, *ACS Omega* **2020**, *5*, 10366.
[19] Y. Hu, J. Liao, D. Wang, G. Li, *Anal. Chem.* **2014**, *86*, 3955.
[20] V. K. Rao, T. P. Radhakrishnan, *ACS Appl. Mater. Interfaces* **2015**, *7*, 12767.
[21] H. W. Chang, Y. C. Tsai, C. W. Cheng, C. Y. Lin, Y. W. Lin, T. M. Wu, *J. Colloid Interface Sci.* **2011**, *360*, 305.
[22] R. Buividas, P. R. Stoddart, S. Juodkazis, *Ann. Phys.* **2012**, *524*, L5.
[23] I. Izquierdo-Lorenzo, S. Jradi, P. M. Adam, *RSC Adv.* **2014**, *4*, 4128.
[24] G. Pavliuk, D. Pavlov, E. Mitsai, O. Vitrik, A. Mironenko, A. Zakharenko, S. A. Kulinich, S. Juodkazis, S. Bratskaya, A. Zhizhchenko, A. Kuchmizhak, *Nanomaterials* **2020**, *10*, 49.
[25] J. Mu, J. Li, W. Li, S. Sun, W. Sun, C. Gu, *Appl. Phys. B: Lasers Opt.* **2014**, *117*, 121.
[26] S. Bai, D. Serien, Y. Ma, K. Obata, K. Sugioka, *ACS Appl. Mater. Interfaces* **2020**, *12*, 42328.
[27] F. İdikut, B. Karagöz, A. Bek, *Advances in Optics: Reviews* (Ed: S. Y. Yurish), IFSA, Barcelona, Spain **2021**.
[28] K. V. Sreekanth, J. K. Chua, V. M. Murukeshan, *Appl. Opt.* **2010**, *49*, 6710.
[29] T. Ito, S. Okazaki, *Nature* **2000**, *406*, 1027.
[30] M. Birnbaum, *J. Appl. Phys.* **1965**, *36*, 3688.
[31] D. C. Emmony, R. P. Howson, L. J. Willis, *Appl. Phys. Lett.* **1973**, *23*, 598.
[32] C. Zwahr, A. Welle, T. Weingärtner, C. Heinemann, B. Kruppke, N. Gulow, M. G. Holthaus, A. F. Lasagni, *Adv. Eng. Mater.* **2019**, *21*, 1900639.
[33] X. Shi, X. Xu, *Appl. Phys. A: Mater. Sci. Process.* **2019**, *125*, 256.
[34] D. Tan, K. N. Sharafudeen, Y. Yue, J. Qiu, *Prog. Mater. Sci.* **2016**, *76*, 154.
[35] J. Bonse, S. Höhm, S. V. Kirner, A. Rosenfeld, J. Krüger, *IEEE J. Sel. Top. Quantum Electron.* **2017**, *23*, 9000615.
[36] C.-H. Lin, L. Jiang, Y.-H. Chai, H. Xiao, S.-J. Chen, H.-L. Tsai, *Opt. Express* **2009**, *17*, 21581.
[37] E. D. Diebold, N. H. Mack, S. K. Doorn, E. Mazur, *Langmuir* **2009**, *25*, 1790.
[38] R. Buividas, P. R. Stoddart, S. Juodkazis, *Ann. Phys.* **2012**, *524*, L5.
[39] S. Hamad, S. S. Bharati Moram, B. Yendeti, G. K. Podagatlapalli, S. V. S. Nageswara Rao, A. P. Pathak, M. A. Mohiddon, V. R. Soma, *ACS Omega* **2018**, *3*, 18420.
[40] R. K. Avasarala, T. Jena, S. K. Balivada, C. Angani, H. Syed, V. R. Soma, G. K. Podagatlapalli, *Results Opt.* **2021**, *5*, 100153.
[41] Y. Borodaenko, S. Syubaev, S. Gurbatov, A. Zhizhchenko, A. Porfirev, S. Khonina, E. Mitsai, A. V. Gerasimenko, A. Shevlyagin, E. Modin, S. Juodkazis, E. L. Gurevich, A. A. Kuchmizhak, *ACS Appl. Mater. Interfaces* **2021**, *13*, 54551.
[42] J. Bonse, H. Sturm, D. Schmidt, W. Kautek, *Appl. Phys. A: Mater. Sci. Process.* **2000**, *71*, 657.
[43] J. Reif, F. Costache, M. Henyk, S. V. Pandelov, *Appl. Surf. Sci.* **2002**, *197–198*, 891.
[44] A. Borowiec, H. K. Haugen, *Appl. Phys. Lett.* **2003**, *82*, 4462.
[45] J. Reif, O. Varlamova, S. Varlamov, M. Bestehorn, *Appl. Phys. A: Mater. Sci. Process.* **2011**, *104*, 969.
[46] Z. Li, Q. Wu, X. Jiang, X. Zhou, Y. Liu, X. Hu, J. Zhang, J. Yao, J. Xu, *Appl. Surf. Sci.* **2021**, *580*, 152107.
[47] J. Sipe, J. Young, J. Preston, H. Van Driel, *Phys. Rev. B* **1983**, *27*, 1141.
[48] F. Keilmann, Y. H. Bai, *Appl. Phys. A* **1982**, *29*, 9.
[49] J. Bonse, A. Rosenfeld, J. Krüger, *J. Appl. Phys.* **2009**, *106*, 104910.
[50] B. Öktem, I. Pavlov, S. Ilday, H. Kalaycıoğlu, A. Rybak, S. Yavaş, M. Erdoğan, F. Ö. Ilday, *Nat. Photonics* **2013**, *7*, 897.
[51] F. İdikut, M. Borra, N. Esmaeilzad, A. Bek, *Proc. of the 2nd Int. Conf. on Optics, Photonics and Lasers (OPAL)*, IFSA Publishing, Barcelona **2019**, p. 69.
[52] O. Tokel, A. Turnalı, G. Makey, P. Elahi, T. Çolakoğlu, E. Ergeçen, Ö. Yavuz, R. Hübner, M. Z. Borra, I. Pavlov, A. Bek, R. Turan, D. K. Kesim, S. Tozburun, S. İlday, F. Ö. İlday, *Nat. Photonics* **2017**, *11*, 639.
[53] L. Liu, P. Peng, A. Hu, G. Zou, W. W. Duley, Y. N. Zhou, *Appl. Phys. Lett.* **2013**, *102*, 073107.
[54] S. Abdul Jalil, J. Yang, M. Elkabbash, C. Cong, C. Guo, *Appl. Phys. Lett.* **2019**, *115*, 031601.
[55] B. Bin Xu, Z. C. Ma, L. Wang, R. Zhang, L. G. Niu, Z. Yang, Y. L. Zhang, W. H. Zheng, B. Zhao, Y. Xu, Q. D. Chen, H. Xia, H. B. Sun, *Lab Chip* **2011**, *11*, 3347.
[56] S. Pavlova, H. Rezaei, I. Pavlov, H. Kalaycıoğlu, F. Ö. İlday, *Appl. Phys. B* **2018**, *10*, 124.
[57] S. Mingu, I. Pavlov, C. D. Son, A. Bek, in *Proc. of the 13th Int. Joint Conf. on Biomedical Engineering Systems and Technologies*, Scitepress, Setubal, Vol. *2*, **2020**, p. 192.
[58] I. Persaud, W. E. L. Grossman, *J. Raman Spectrosc.* **1993**, *24*, 107.
[59] H. Raether, Surface Plasmons on Smooth and Rough Surfaces and on Gratings, Springer-Verlag Berlin, Heidelberg **1988**.
[60] J. Perumal, K. V. Kong, U. S. Dinish, R. M. Bakker, M. Olivo, *RSC Adv.* **2014**, *4*, 12995.
[61] C. Lee, C. Robertson, A. Nguyen, M. Kahraman, S. Wachsmann-Hogiu, *Sci. Rep.* **2015**, *5*, 11644.
[62] W. Meng, F. Hu, L. Y. Zhang, X. H. Jiang, L. De Lu, X. Wang, *J. Mol. Struct.* **2013**, *1035*, 326.
[63] K. Kneipp, Y. Wang, H. Kneipp, I. Itzkan, R. R. Dasari, M. S. Feld, *Phys. Rev. Lett.* **1996**, *76*, 2444.
[64] A. Kudelski, *Chem. Phys. Lett.* **2005**, *414*, 271.
[65] A. Akbıyık, N. Avishan, Ö. Demirtaş, A. K. Demir, E. Yüce, A. Bek, *Adv. Opt. Mater.* **2022**, *10*, 2200114.
[66] *Detailed Explanation of the Finite Element Method (FEM)*, https://www.comsol.com/multiphysics/finite-element-method (accessed: January 2022).
[67] W. Ahmed, Ö. Demirtaş, İ. M. Öztürk, A. Bek, *ACS Appl. Nano Mater.* **2020**, *3*, 6766.
[68] E. Kovalska, I. Pavlov, P. Deminskyi, A. Baldycheva, F. Ö. Ilday, C. Kocabas, *ACS Omega* **2018**, *3*, 1546.
[69] P. B. Johnson, R. W. Christy, *Phys. Rev. B* **1972**, *6*, 4370.